MNRAS **000**, 1–15 (2020) Preprint 18 February 2022 Compiled using MNRAS LATEX style file v3.0

Star-disk alignment in the protoplanetary disks: SPH simulation of the collapse of turbulent molecular cloud cores

Daisuke Takaishi,[1]★ Yusuke Tsukamoto,[1] and Yasushi Suto[2,3]
[1] *Graduate School of Science and Engineering, Kagoshima University, Kagoshima 890-0065, Japan*
[2] *Department of Physics, The University of Tokyo, Tokyo 113-0033, Japan*
[3] *Research Center for the Early Universe, School of Science, The University of Tokyo, Tokyo 113-0033, Japan*

arXiv:2001.05456v1 [astro-ph.EP] 15 Jan 2020

Accepted 2020 January 14. Received 2020 January 8; in original form 2019 August 10

ABSTRACT

We perform a series of three-dimensional smoothed particle hydrodynamics (SPH) simulations to study the evolution of the angle between the protostellar spin and the protoplanetary disk rotation axes (the star-disk angle $\psi_{\rm sd}$) in turbulent molecular cloud cores. While $\psi_{\rm sd}$ at the protostar formation epoch exhibits broad distribution up to $\sim 130^\circ$, $\psi_{\rm sd}$ decreases ($\lesssim 20^\circ$) in a timescale of $\sim 10^4$ yr. This timescale of the star-disk alignment, $t_{\rm alignment}$, corresponds basically to the mass doubling time of the central protostar, in which the protostar forgets its initial spin direction due to the mass accretion from the disk. Values of $\psi_{\rm sd}$ both at $t = 10^2$ yr and $t = 10^5$ yr after the protostar formation are independent of the ratios of thermal and turbulent energies to gravitational energy of the initial cloud cores: $\alpha = E_{\rm thermal}/|E_{\rm gravity}|$ and $\gamma_{\rm turb} = E_{\rm turbulence}/|E_{\rm gravity}|$. We also find that a warped disk is possibly formed by the turbulent accretion flow from the circumstellar envelope.

Key words: turbulence – hydrodynamics – protoplanetary discs – stars: protostars – methods: numerical

1 INTRODUCTION

Observed exoplanetary systems have exhibited unexpectedly broad diversities (Winn & Fabrycky 2015). One of the intriguing discoveries is the fact that approximately 20% of hot Jupiter have orbital planes misaligned relative to the spin axis of their host stars. For instance, Kamiaka et al. (2019) shows that 28 out of 124 transiting close-in gas-giant planets have the projected spin-orbit angle λ exceeding 30° via the Rossiter McLaughlin (RM) effect (Rossiter 1924; McLaughlin 1924; Queloz et al. 2000; Ohta et al. 2005; Winn et al. 2005; Hirano et al. 2011; Albrecht et al. 2012; Triaud 2018).

The origin of the large spin-orbit angle remains unclear. One of the promising mechanism is the dynamical evolution of the orbital plane by planet-planet and star-planet interactions. Because the RM effect has been preferentially observed for short-period and giant planets, the violent dynamical evolution such as the planetary migration (e.g., Lin et al. 1996; Alibert et al. 2005), planet-planet scattering (e.g., Rasio & Ford 1996; Nagasawa et al. 2008; Nagasawa & Ida 2011; Beaugé & Nesvorný 2012), and strong perturbation due to distant outer objects (e.g., Kozai 1962; Lidov 1962; Fabrycky & Tremaine 2007; Batygin 2012; Xue et al. 2014; Anderson et al. 2016; Xue & Suto 2016) possibly explains the large spin-orbit angle. According to these mechanisms, multi-planetary transiting systems which have almost co-planar orbital planes may not have the significant star-planet misalignment because the violent dynamical evolution also causes the misalignment between the orbital planes of planets. Consistent with this expectation, Kepler-89 (with four transiting planets) and Kepler-25 (with two transiting and one non-transiting planets) are suggested to have $\lambda \sim 0$ from the RM observations by Hirano et al. (2012) and Albrecht et al. (2013), respectively.

On the other hand, however, there is a transiting multi-planetary system, Kepler-56, which has a significant oblique stellar spin although the planets in the system have almost co-planer orbits; Huber et al. (2013) showed that its stellar inclination angle i_s is $\sim 45^\circ$ from the asteroseismic analysis. While it could be explained by some kind of perturbation that changes the two planetary orbits in a coherent fashion, it seems natural to interpret it in terms of a primordial origin. For instance, the stellar spin axis may be significantly misaligned with the protoplanetary disk rotation axis.

★ E-mail: k3790238@kadai.jp (D. Takaishi)

© 2020 The Authors

This possibility has been investigated in several previous studies. Bate et al. (2010) approached the problem using smoothed particle hydrodynamics (SPH) combined with the sink particle technique. Specifically they followed evolution of a relative angle between the stellar spin and the protoplanetary disk rotation axes (hereafter, the star-disk angle $\psi_{\rm sd}$) in a star cluster that forms from a supersonic turbulent molecular cloud with its mass, size, and Mach number being $50\,M_\odot$, 0.375 pc (=77400 au), and $\mathcal{M}$ = 6.4, respectively. Although the star-disk angle $\psi_{\rm sd}$ can be misaligned via the stellar close-encounter in a multiple star-forming region, they pointed out that such events are rare and the orientations of the disk and star tends to be aligned in most cases. Furthermore, they suggested that the reliable prediction of the star-disk angle distribution is not easy because the process occurs in an inherently chaotic environment of the cluster forming region.

More recently, Fielding et al. (2015) examined the evolution of the star-disk angle $\psi_{\rm sd}$ in a massive molecular cloud with supersonic turbulence, which has the mass, size, and Mach number of $150\,M_\odot$, 0.397 pc (=81920 au), and $\mathcal{M}$ = 7.5, respectively. They performed the hydrodynamic and magnetohydrodynamic simulations with the grid-based adaptive mesh refinement (AMR), and indicated that the large star-disk angles around 40° are more common. This results are consistent with the observed spin-orbit angle distribution of hot Jupiters. They confirmed that the gravitational torque from the protoplanetary disk to the stellar quadrupole does not wipe out the misalignment as long as the spin rate of the protostar is significantly slower than the breakup rotation rate.

Both papers mentioned above focused on massive compact molecular clouds with supersonic turbulence, which correspond to star-cluster forming regions such as the Orion Nebula Cluster (e.g., Hillenbrand 1997) and infrared-dark clouds (Butler & Tan 2012). In nearby star-forming regions such as the Taurus molecular cloud, however, a relatively compact and isolated protostar forms from a low mass molecular cloud core. For instance, the pre-stellar core L1544 is estimated to have mass of $\sim 1.3\,M_\odot$, number density of $\sim 4.9\times10^5$ cm^{-3}, size of ~ 0.021 pc, and velocity dispersion of ~ 0.28 km s^{-1} (e.g., Tafalla et al. 1998; Williams et al. 1999; Crutcher et al. 2004; Ward-Thompson et al. 2007). Therefore, the significant difference of the environment between star-cluster forming regions and the nearby star-forming region may affect the distribution of the star-disk angle.

In this paper, we focus on isolated turbulent molecular cloud cores with typical sizes of 0.01-0.1 pc ($\sim 1000 - 10000$ au) that have not yet been explored in the above studies. Because several observations suggest that the molecular cloud cores have weak turbulence of $\mathcal{M} < 1$ (e.g., Andre et al. 1996; Ward-Thompson et al. 2007), we consider sub- to trans-sonic turbulent molecular cloud cores and examine the evolution of $\psi_{\rm sd}$, the angle between the protostar spin and the protoplanetary disk rotation axes.

We neglect the magnetic field and start our simulations from a spherically symmetric isothermal cloud core with the turbulent motion following the power spectrum of $P_v(k) \propto k^{-4}$. We perform 26 different simulations by varying their initial thermal and turbulent energies. We use the sink particle technique to represent protostars, and examine the star and disk evolution for approximately 10^5 yr after the protostar formation.

The structure of this paper is as follows. Section 2 describes our numerical method and initial conditions for the SPH simulation. Section 3 discusses the results of our fiducial model in detail, with particular attention to the evolution of the relative angles of orientations of the protostar, protoplanetary disk, and the surrounding envelope component. Statistical analysis for 20 models having a single protostar is presented in Section 4. Further implications of the present simulation are discussed in Section 5, and finally Section 6 is devoted to the conclusion of this paper.

2 NUMERICAL METHOD AND INITIAL CONDITIONS OF THE SIMULATIONS

2.1 Numerical Method

We solve equations of hydrodynamics including self-gravity with the smoothed particle hydrodynamics (SPH) method (Lucy 1977; Gingold & Monaghan 1977; Monaghan & Lattanzio 1985),

$$\frac{D\boldsymbol{v}}{Dt} = -\frac{1}{\rho}\nabla P - \nabla\phi, \tag{1}$$

$$\nabla^2\phi = 4\pi G\rho, \tag{2}$$

where ρ is the gas density, $\boldsymbol{v}$ is the gas velocity, P is the gas pressure, ϕ is the gravitational potential and G is the gravitational constant. The SPH code that we use here has been applied for a variety of problems (e.g., Tsukamoto & Machida 2011, 2013; Tsukamoto et al. 2013, 2015a,b,c; Yoneda et al. 2016; Tsukamoto et al. 2017, 2018).

We adopt the barotropic equation of state,

$$P = c_{\rm s,0}^2\rho\left[1+\left(\frac{\rho}{\rho_{\rm c}}\right)^{2/5}\right], \tag{3}$$

where $c_{\rm s,0} = 1.9\times10^4$ cm s^{-1} is the sound velocity at the temperature of 10 K and $\rho_{\rm c} = 4\times10^{-14}$ g cm^{-3} is the critical density at which the thermal evolution changes from the isothermal to adiabatic. This empirical equation of state is adopted in previous disk formation simulations neglecting the radiation transfer (e.g., Machida et al. 2007, 2010; Tsukamoto & Machida 2013). The molecular cloud core is assumed to have an initial temperature of T = 10 K at which the cosmic-ray heating is balanced with the cooling of the molecular line emissions and dust continuum emissions (e.g., McKee & Ostriker 2007; Yamamoto 2017).

The main purpose of the present study is to examine the angle between the stellar spin and the disk rotation axes $\psi_{\rm sd}$. However, it is impossible to numerically resolve the central protostar. Therefore we adopt the sink particle technique (Bate et al. 1995) and regard the mass and spin direction of the sink particle as those of the protostar. We create a sink particle when the density of SPH particle reaches the threshold value $\rho_{\rm sink} = 4\times10^{-8}$ g cm^{-3}, which corresponds to the density when the second collapse begins (e.g., Masunaga & Inutsuka 2000; Inutsuka 2012). The sink particle interacts with SPH particles through gravity. We set the accretion radius of the sink particle as $r_{\rm acc}$ = 1 au, and all the SPH particles within the accretion radius are removed, and their

mass, linear momentum, and angular momentum with respect to the sink particle are added to the sink particle. The accretion radius of 1 au can reasonably resolve the formation and early evolution of the protoplanetary disk (Machida et al. 2014). Note that this accretion radius is much smaller than 5 au adopted by Bate et al. (2010).

We simply add the accreted mass and angular momentum to the sink particle. While this procedure conserves the angular momentum within the radius of 1 au represented by the sink particle, it should *not* be identified with the spin angular momentum of the protostar itself because it exceeds the breakup value. Bate et al. (2010) and Fielding et al. (2015) proposed different schemes of estimating the stellar spin on the basis of the imposed sub-grid physics. As described in the next subsection, we implemented the procedure by Fielding et al. (2015), and re-simulated one of the model. We confirmed that their scheme significantly suppresses the amplitude of the spin, but that its direction is almost unchanged. Therefore, we decided to use the total angular momentum vector within the radius of 1 au from the sink particle as a good proxy for the *direction* of the central stellar spin.

2.2 Initial Conditions

The hydrodynamic simulations with both magnetic field and turbulence are computationally very demanding, and it is not easy to perform the parameter study as attempted below. Thus we decide to ignore the magnetic field in the present simulation, and focus on the effect of the turbulence on the spin-orbit architecture of the protoplanetary disks. The simulation follows approximately 10^5 yr after the protostar formation. We plan to incorporate the magnetic field in the subsequent work.

For the initial condition, we adopt spherically symmetric and isothermal cloud cores with the turbulent velocity field which obeys the velocity power spectrum of $P_v(k) \propto k^{-4}$ (Goodman et al. 1993; Barranco & Goodman 1998; Burkert & Bodenheimer 2000). The total mass of the cloud core is fixed to be $1M_\odot$. The number of SPH particles is $N_\mathrm{p} \sim 10^6$ and the mass of SPH particles is set to be $m_\mathrm{sph} = 1M_\odot/N_\mathrm{p} = 10^{-6}M_\odot$. Bate & Burkert (1997) reported that the reliable SPH simulation of the could core collapse needs to resolve the local Jeans mass, and requires $N_p \gg 10^4$. Thus our current resolution is significantly better than the criterion.

Molecular cloud cores are parameterized with two parameters α and γ_turb. Following Miyama et al. (1984), α is defined as

$$\alpha = \frac{E_\mathrm{thermal}}{|E_\mathrm{grav}|}, \tag{4}$$

where $E_\mathrm{thermal} = 3c_{\mathrm{s},0}^2 M_\odot/2$ and $E_\mathrm{grav} = -3GM_\odot^2/5R_\mathrm{init}$ are the thermal and gravitational energies corresponding to a homogeneous sphere of $1M_\odot$. Then the initial radius of the cloud core, R_init is written as

$$R_\mathrm{init} = \frac{2GM_\odot}{5c_{\mathrm{s},0}^2}\alpha. \tag{5}$$

The relative strength of the turbulence is parameterized by the virial parameter γ_turb defined Bertoldi & McKee (1992). More specifically, it is given by the ratio of the turbulence and gravitational energies of the initial cloud:

$$\gamma_\mathrm{turb} = \frac{E_\mathrm{turb}}{|E_\mathrm{grav}|} = \frac{5\sigma_\mathrm{v}^2 R_\mathrm{init}}{2GM_\odot}, \tag{6}$$

where $E_\mathrm{turb} = 3\sigma_\mathrm{v}^2 M_\odot/2$ with σ_v being the one-dimensional velocity dispersion of the turbulent molecular cloud core.

We consider 26 models specified by the different set of α and γ_turb (see Figure 1 and Table 1). We impose $\alpha+\gamma_\mathrm{turb} \lesssim 0.8$ because the cloud cores are supposed to be nearly virialized in reality. We do not assign the angular momentum of the initial core *a priori*. Due to the stochastic nature of the turbulent velocity field, however, the core acquires a non-vanishing net angular momentum $\boldsymbol{J}_\mathrm{init}$. Thus we set the direction of $\boldsymbol{J}_\mathrm{init}$ as the z-axis of each simulation model.

Table 1 lists the dimensionless angular momentum of the core:

$$\beta_\mathrm{eff} = \frac{25}{12}\frac{|\boldsymbol{J}_\mathrm{init}|^2}{GM_\odot^3 R_\mathrm{init}}, \tag{7}$$

and other parameters for each model:

$$\rho_\mathrm{init} = \frac{3M_\odot}{4\pi R_\mathrm{init}^3}, \tag{8}$$

$$t_\mathrm{ff} = \sqrt{\frac{3\pi}{32G\rho_\mathrm{init}}}, \tag{9}$$

$$\mathcal{M} = \frac{1}{c_{\mathrm{s},0}}\sqrt{\frac{1}{N_\mathrm{p}}\sum_{i=1}^{N_\mathrm{p}} v_{i,\mathrm{SPH}}^2}, \tag{10}$$

where ρ_init, t_ff, and $\mathcal{M}$ are the density, free-fall time, and mean Mach number of the initial cloud core, respectively. The last column of Table 1 indicates the multiplicity of the protostars formed at the end of our simulation $\sim 10^5$ yr.

2.3 Definitions of Protostar, Disk and Envelope in our Simulation

The estimate of the star-disk angle crucially depends on the definition of the protostar and disk in the simulations. Our SPH simulation resolves the spatial structure of the disk very well, but not the protostar *at all*. Instead, we adopt a sink particle technique to identify a 1 au sphere enclosing the protostar. The mass, velocity and angular momentum of the sink particle, $M_\mathrm{s}(t)$, $\boldsymbol{v}_\mathrm{s}(t)$ and $\boldsymbol{J}_\mathrm{s}(t)$, can be directly computed from simulations. Nevertheless they are not identical to those of the protostar that is supposed to occupy merely the central $\sim 5\times10^{-3}$ au scale. In particular, it is well known that a substantial fraction of $\boldsymbol{J}_\mathrm{s}(t)$ should be removed from the region since it would exceed the breakup value of the stellar surface otherwise.

Indeed, several numerical schemes have been proposed to empirically limit the amount of the angular momentum accreted onto the central protostar (Bate et al. 2010; Fielding et al. 2015). For instance, Bate et al. (2010) were interested in the reorientation channel of the inner disk and the central protostar by the warp propagation, and assumed that the protostar (sink particle) acquires the mass and angular momentum transported through the protoplanetary disk alone. Fielding et al. (2015), on the other hand, did not allow that the accreted angular momentum exceeds the

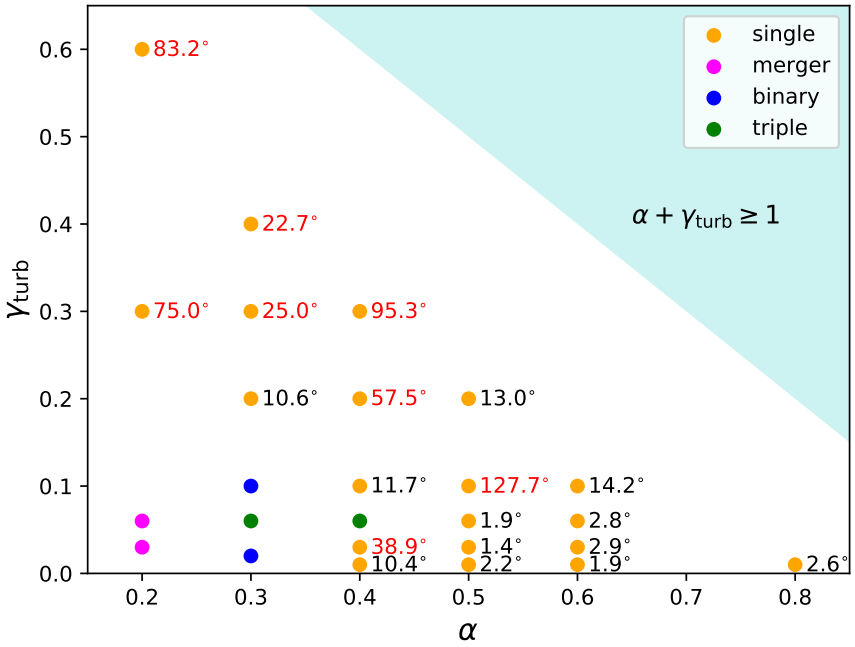


Figure 1. (α, $\gamma_{\rm turb}$) of the models. The upper-right shaded region corresponds to gravitationally unbound cloud cores. The multiplicity of the protostars is shown with different colors. The numbers at each point indicate the initial star-disk angle $\psi_{\rm sd}$ at the formation epoch of the sink particle for single star cases. Models with $\psi_{\rm sd} > 20°$ are indicated with red numbers.

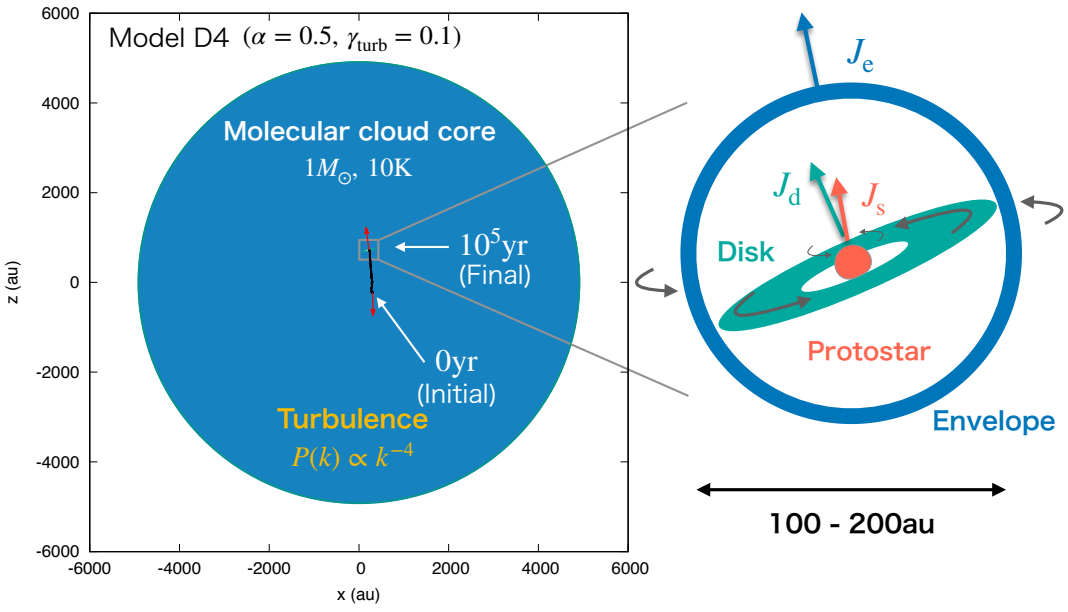


Figure 2. Schematic illustration of the configuration of the initial cloud core, circumstellar envelope, protoplanetary disk and protostar in model D4. $\boldsymbol{J}_{\rm s}$, $\boldsymbol{J}_{\rm d}$ and $\boldsymbol{J}_{\rm e}$ are the angular momentum of the protostar spin, protoplanetary disk rotation and circumstellar envelope rotation, respectively. Two red arrows in the left figure show $\boldsymbol{J}_{\rm s}$ at $t = 0$ yr and $t = 10^5$ yr.

breakup value of the stellar spin, since they were interested in the star-disk alignment mechanism due to the gravitational torque between the spin-induced stellar quadrupole and the surrounding disk.

As briefly mentioned in the previous section, we re-simulated one of the model following the sub-grid procedure of Fielding et al. (2015). We made sure that the final star-disk angle $\psi_{\rm sd}$ is well converged to the value without implementing the procedure, while the amplitude of the stellar spin is significantly suppressed. In addition, as shown by Bate (2018), the star-disk misalignment can be captured even without the sub-grid model in the calculation of the

Table 1. The model names and parameters which characterize the initial molecular cloud core; $\alpha = E_{\rm thermal}/|E_{\rm grav}|$, $\gamma_{\rm turb} = E_{\rm turb}/|E_{\rm grav}|$, $\beta_{\rm eff}$ is the dimensionless angular momentum, $R_{\rm init}$ and $\rho_{\rm init} = 3M_{\rm init}/(4\pi R_{\rm init}^3)$ are the initial radius and density of the cloud cores, $\mathcal{M}$ is the mean Mach number, $t_{\rm ff} = \sqrt{3\pi/(32G\rho_{\rm init})}$ is the free-fall time of the initial cloud cores, $\psi_{\rm sd}(t = 10^2{\rm yr})$ and $\psi_{\rm sd}(t = 10^5{\rm yr})$ are the star-disk angles measured at $t = 10^2$ yr and $t = 10^5$ yr from the protostar formation epoch. The last column indicates the multiplicity of the protostars in the simulation. See subsection 2.2 for further detail.

Model	α	$\gamma_{\rm turb}$	$\beta_{\rm eff}$	$R_{\rm init}$ [au]	$\rho_{\rm init}$ [g cm^{-3}]	$\mathcal{M}$	$t_{\rm ff}$ [yr]	$\psi_{\rm sd}(t = 10^2{\rm yr})$	$\psi_{\rm sd}(t = 10^5{\rm yr})$	multiplicity
A1	0.2	0.03	0.0036	1967	1.9×10^{-17}	0.67	1.5×10^4	–	–	single(merger)
A2	0.2	0.06	0.0072	1967	1.9×10^{-17}	0.95	1.5×10^4	–	–	single(merger)
A3	0.2	0.3	0.036	1967	1.9×10^{-17}	2.1	1.5×10^4	75.0°	11.0°	single
A4	0.2	0.6	0.072	1967	1.9×10^{-17}	3.0	1.5×10^4	83.2°	8.6°	single
B1	0.3	0.02	0.0024	2950	5.5×10^{-18}	0.45	2.8×10^4	–	–	binary
B2	0.3	0.06	0.0072	2950	5.5×10^{-18}	0.77	2.8×10^4	–	–	triple
B3	0.3	0.1	0.012	2950	5.5×10^{-18}	1.0	2.8×10^4	–	–	binary
B4	0.3	0.2	0.024	2950	5.5×10^{-18}	1.4	2.8×10^4	10.6°	10.0°	single
B5	0.3	0.3	0.036	2950	5.5×10^{-18}	1.7	2.8×10^4	25.0°	14.2°	single
B6	0.3	0.4	0.048	2950	5.5×10^{-18}	2.0	2.8×10^4	22.7°	10.2°	single
C1	0.4	0.01	0.0012	3933	2.3×10^{-18}	0.27	4.3×10^4	10.4°	5.2°	single
C2	0.4	0.03	0.0036	3933	2.3×10^{-18}	0.47	4.3×10^4	38.9°	3.9°	single
C3	0.4	0.06	0.0072	3933	2.3×10^{-18}	0.67	4.3×10^4	–	–	triple
C4	0.4	0.1	0.012	3933	2.3×10^{-18}	0.87	4.3×10^4	11.7°	6.0°	single
C5	0.4	0.2	0.024	3933	2.3×10^{-18}	1.2	4.3×10^4	57.5°	8.4°	single
C6	0.4	0.3	0.036	3933	2.3×10^{-18}	1.5	4.3×10^4	95.3°	7.2°	single
D1	0.5	0.01	0.0012	4917	1.2×10^{-18}	0.24	6.1×10^4	2.2°	2.5°	single
D2	0.5	0.03	0.0036	4917	1.2×10^{-18}	0.42	6.1×10^4	1.4°	5.6°	single
D3	0.5	0.06	0.0072	4917	1.2×10^{-18}	0.60	6.1×10^4	1.9°	6.5°	single
D4	0.5	0.1	0.012	4917	1.2×10^{-18}	0.77	6.1×10^4	127.7°	8.7°	single
D5	0.5	0.2	0.024	4917	1.2×10^{-18}	1.1	6.1×10^4	13.0°	14.2°	single
E1	0.6	0.01	0.0012	5900	6.9×10^{-19}	0.22	8.0×10^4	1.9°	6.8°	single
E2	0.6	0.03	0.0036	5900	6.9×10^{-19}	0.39	8.0×10^4	2.9°	5.2°	single
E3	0.6	0.06	0.0072	5900	6.9×10^{-19}	0.55	8.0×10^4	2.8°	7.8°	single
E4	0.6	0.1	0.012	5900	6.9×10^{-19}	0.71	8.0×10^4	14.2°	7.5°	single
F1	0.8	0.01	0.0012	7866	2.9×10^{-19}	0.19	1.2×10^5	2.6°	1.2°	single

star cluster formation. Therefore, we do not introduce the sub-grid model in what follows.

We define the protoplanetary disk as a set of SPH particles that satisfy the following criteria:

$$\frac{1}{2}v_{i,\rm SPH}^2 - \frac{GM_{\rm s}}{|\boldsymbol{r}_{i,\rm SPH} - \boldsymbol{r}_{\rm s}|} < 0, \tag{11}$$

$$2\,|(\boldsymbol{v}_{i,\rm SPH} - \boldsymbol{v}_{\rm s})_r| < |(\boldsymbol{v}_{i,\rm SPH} - \boldsymbol{v}_{\rm s})_t|, \tag{12}$$

$$|\boldsymbol{r}_{i,\rm SPH} - \boldsymbol{r}_{\rm s}| < r_{\rm limit} = 500\ {\rm au}, \tag{13}$$

where the subscripts r and t denoting the radial and tangential components of the relative velocity. Equation (11) checks whether the SPH particles is bound to a sink particle. Equation (12), which checks whether the rotation of the SPH particle is much faster than the infall, is introduced to define the rotation plane of the disk more precisely. The disk rotation axis fluctuates without this condition. Equation (13) introduces the maximum size of the disk. We confirm, however, that the real size of the disk is determined by equations (11) and (12), and our result is not changed by the choice of $r_{\rm limit}$ between 200 to 500 au.

Finally we define the circumstellar envelope surrounding the protoplanetary disk. In this paper, the envelope is defined as a set of all the SPH particles within 2000 au from the sink particle. Hence, the envelope also includes the disk gas.

Adopting the above definitions of the protostar, protoplanetary disk, and circumstellar envelope, we compute the angular momenta of the protostar spin, protoplanetary disk rotation, and circumstellar envelope rotation, $\boldsymbol{J}_{\rm s}$, $\boldsymbol{J}_{\rm d}$, and $\boldsymbol{J}_{\rm e}$, at each epoch. The relative angles between $\boldsymbol{J}_{\rm s}$, $\boldsymbol{J}_{\rm d}$, and $\boldsymbol{J}_{\rm e}$ are defined as

$$\psi_{\rm sd} = \cos^{-1}\left(\frac{\boldsymbol{J}_{\rm s}\cdot\boldsymbol{J}_{\rm d}}{|\boldsymbol{J}_{\rm s}||\boldsymbol{J}_{\rm d}|}\right), \tag{14}$$

$$\psi_{\rm se} = \cos^{-1}\left(\frac{\boldsymbol{J}_{\rm s}\cdot\boldsymbol{J}_{\rm e}}{|\boldsymbol{J}_{\rm s}||\boldsymbol{J}_{\rm e}|}\right), \tag{15}$$

$$\psi_{\rm de} = \cos^{-1}\left(\frac{\boldsymbol{J}_{\rm d}\cdot\boldsymbol{J}_{\rm e}}{|\boldsymbol{J}_{\rm d}||\boldsymbol{J}_{\rm e}|}\right). \tag{16}$$

We mainly investigate the time evolution of these angles in this paper.

3 EVOLUTION OF $\psi_{\rm sd}$, $\psi_{\rm se}$ AND $\psi_{\rm de}$ FOR OUR FIDUCIAL MODEL

Before proceeding to the statistical analysis, we focus on model D4 that represents a virialized ($\alpha = 0.5$) and reasonably strong but still subsonic turbulence ($\mathcal{M} = 0.77$). Thus we adopt this model as our fiducial example, and discuss its detailed evolutionary behavior in this section.

Figure 2 schematically illustrates the configuration of our simulation result for model D4 ($\alpha = 0.5$, $\gamma_{\rm turb} = 0.1$) . The simulation starts from the molecular cloud core with the radius of ~ 5000 au. The molecular cloud core immediately gravitationally collapses, and the sink particle forms close

to the center of the initial cloud core. We define the origin of the time $t = 0$ as at the formation epoch of the protostar. The spin of the sink particle shown with red arrow is initially almost anti-parallel to the z-axis. The trajectory of the sink particle during the evolution is indicated by the black curve, and its spin shown with red arrow becomes aligned after 10^5 yr. The close-up schematic figure of the system in Figure 2 shows the configuration of the angular momentum of the protostar, protoplanetary disk, and circumstellar envelope at $t = 10^5$ yr.

Figures 3 and 4 shows the surface density evolution on x-z and x-y planes. The position of the sink particle is fixed at the center. We define the formation epoch of the sink particle as the origin of the time.

Figure 3 indicates that, just after the protostar formation, the surface density has the dense filamentary structure (top left panel). As time proceeds, the coherent disk structure develops. Coincidentally, the filamentary structure disappears. This indicates that the mass accretion to the protostar is random at the protostar formation epoch and is mainly from the protoplanetary disk in the later phase.

We also find that the disk rotation axis is gradually changing during the evolution. At the early phase, the disk rotation axis is tilted from z axis (e.g., top middle panel of Figure 3). In subsequent evolution, it gradually becomes aligned to the z-axis. The spiral arms are formed in the bottom-left and bottom-middle panels of Figure 4, which is caused by the gravitational instability.

Figure 5 shows the density weighted line-of-sight velocity along the y-axis. At the formation epoch of the protostar (top-left panel), the regions with positive (red) and negative velocity (blue) is mixed around the protostar, indicating that the turbulent velocity field is maintained around the protostar. As time proceeds, the structure of the rotation becomes coherent, indicating that the rotationally supported disk develops. We note that the filamentary structure in the top panels of Figure 3 is infalling and not outflowing.

Figure 6 shows the time evolution of the directions of the stellar spin, disk rotation and envelope rotation. Because the disk surrounding the protostar becomes well developed $\sim 10^2$ yr after the protostar formation, we plot $\psi_{\rm sd}(t)$, $\psi_{\rm se}(t)$, and $\psi_{\rm de}(t)$ for 10^2 yr $< t < 10^5$ yr. The lower panel shows the angles of the stellar spin, disk rotation, and envelope rotation axes relative to the z-axis; $\psi_{\rm sz}(t)$, $\psi_{\rm dz}(t)$, and $\psi_{\rm ez}(t)$.

By the filamentary mass accretion toward the center in the early evolution phase (top left panel of Figure 3), the $\psi_{\rm sz}$ at the early formation epoch has the large value of $\psi_{\rm sz} \sim 150^\circ$ and the stellar spin is significantly different from the rotation direction of the initial cloud core (z-axis). On the other hand, the larger-scale gas distribution shares the initial cloud core rotation and $\psi_{\rm dz}$ and $\psi_{\rm ez}$ are already small even at $t < 10^3$ yr. As a results, the relative angle between the protostar spin and the protoplanetary disk rotation $\psi_{\rm sd}$ or the envelope rotation $\psi_{\rm se}$ also have large values of $\gtrsim 120^\circ$ meaning that the protostar spin and disk rotation or envelope rotation are highly misaligned.

In the subsequent evolution phase, the protostar spin evolves mainly by the accretion of the angular momentum from the disk, and the $\psi_{\rm sd}$ begins to decrease in $t > 10^3$ yr. Simultaneously, the disk angular momentum evolves via the accretion of the angular momentum from the envelope, and the $\psi_{\rm de}$ decreases.

Because of the angular momentum conservation of the entire system, $\psi_{\rm sz}$, $\psi_{\rm dz}$, $\psi_{\rm ez}$ becomes $\sim 0^\circ$ at $t = 10^5$ yr. All rotation axes eventually align toward the z-axis. Note that $\psi_{\rm sd}$ significantly decreases at $t \sim 10^4$ yr. As we will see bellow, this timescale corresponds to the timescale in which the protostar forget its initial spin angular momentum.

Here, we show that the timescale of the alignment found in Figure 3 corresponds to the mass increase timescale of the protostar. Figure 7 shows the time evolution of the protostar mass $M_{\rm s}$ (top), the mass accretion rate of the protostar $\dot{M}_{\rm s}$ (middle), and the angular momentum of the protostar $J_{\rm s} = |\boldsymbol{J}_{\rm s}|$ (bottom). At $t = 10^2$ yr, the protostar mass is $M_{\rm s} \sim 0.03\,M_\odot$, which is consistent with the Jeans mass of the first core (e.g., Machida et al. 2010). Subsequently, the protostar mass increases by the mass accretion from the disk. As shown in middle panel, the mass accretion rate onto the protostar in $t < 10^4$ yr is $\sim 10^{-5} M_\odot yr^{-1}$. Thus, the protostar mass increases by a factor of three in $\sim 10^4$ yr. This means that the timescale of 10^4 yr corresponds to the mass growth timescale of the protostar.

The bottom panel shows that $J_{\rm s}$ is almost constant in $t < 10^4$ yr. This indicates that the angular momentum supplied by the disk is smaller than the inherent angular momentum of the protostar obtained at its formation. In $t > 10^4$ yr, on the other hand, the angular momentum supplied from the disk dominates the inherent angular momentum of the protostar, meaning that the protostar forgets the initial angular momentum. Note that the stellar radius does not change significantly during the protostar evolution phase, the angular momentum accretion rate is proportional to the mass accretion rate. Thus, we conclude that the alignment timescale of the stellar spin corresponds to the mass growth timescale of the protostar.

With the consideration above, the characteristic timescale of the alignment $t_{\rm align}$ can be estimated as

$$t_{\rm align} = \frac{\varepsilon M_0}{\dot{M}_{\rm s}} \sim 10^4 {\rm yr} \left(\frac{M_0}{3\times 10^{-2}\,M_\odot} \right) \left(\frac{\dot{M}_{\rm s}}{10^{-5}\,M_\odot\ {\rm yr}^{-1}} \right)^{-1} \left(\frac{\varepsilon}{3} \right), \tag{17}$$

where $\varepsilon \sim 2-3$ is an empirical fudge factor. As we will show in §4, the timescale of equation (17) well describes the alignment timescale of other models.

Note that the mass accretion rate of $\dot{M}_{\rm s}$ in the early evolution phase is highly uncertain and the smaller mass accretion rate may realize. If $\dot{M}_{\rm s}$ in the real molecular cloud core is smaller than our simulations, it causes longer $t_{\rm align}$. For example, if we take the smaller mass accretion rate of $\dot{M}_{\rm s} \sim 10^{-6}\,M_\odot$ yr^{-1} as suggested by Shu (1977) and from the recent observations of Class 0/I Young Stellar Objects (YSOs) (e.g., Yen et al. 2017), the alignment timescale $t_{\rm align}$ increases by a factor of 10, and becomes $\sim 10^5$ yr.

4 STATISTICAL ANALYSIS OF $\psi_{\rm sd}$, $\psi_{\rm se}$ AND $\psi_{\rm de}$ AND THEIR DEPENDENCE ON THE MODEL PARAMETERS

The last column of Table 1 indicates the multiplicity of the protostars in each model at $\sim 10^5$ yr after the formation of the first sink particle.

In models A1 and A2, two sink particles are formed,

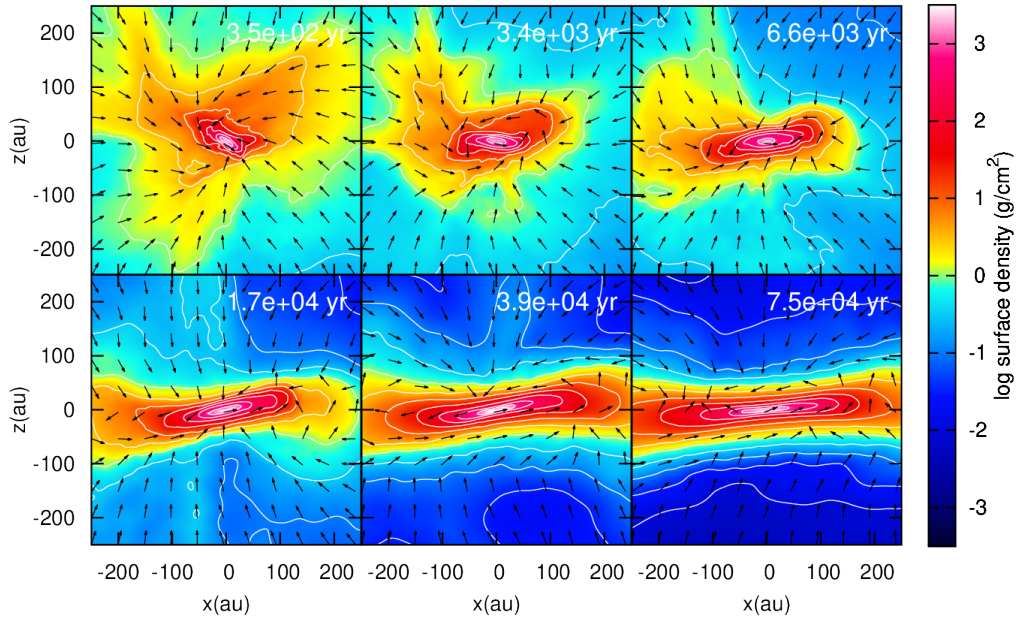


Figure 3. The surface density evolution on the x-z plane for model D4 (α = 0.5, $\gamma_{\rm turb}$ = 0.1) . The top-left, top-middle and top-right panels show snapshots at 3.5×10^2 yr, 3.4×10^3 yr and 6.6×10^3 yr, respectively. The bottom-left, bottom-middle and bottom-right panels show snapshots at 1.7×10^4 yr, 3.9×10^4 yr and 7.5×10^4 yr, respectively. White lines show contours of the surface density. Black arrows show directions of the density weighted velocity.

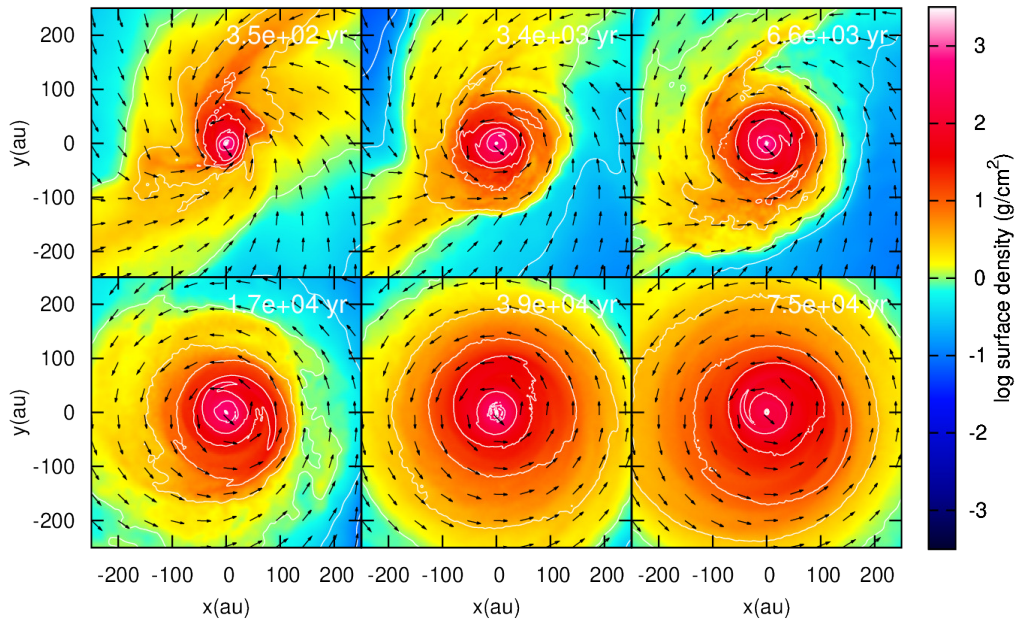


Figure 4. Same as Figure 3 but on x-y plane.

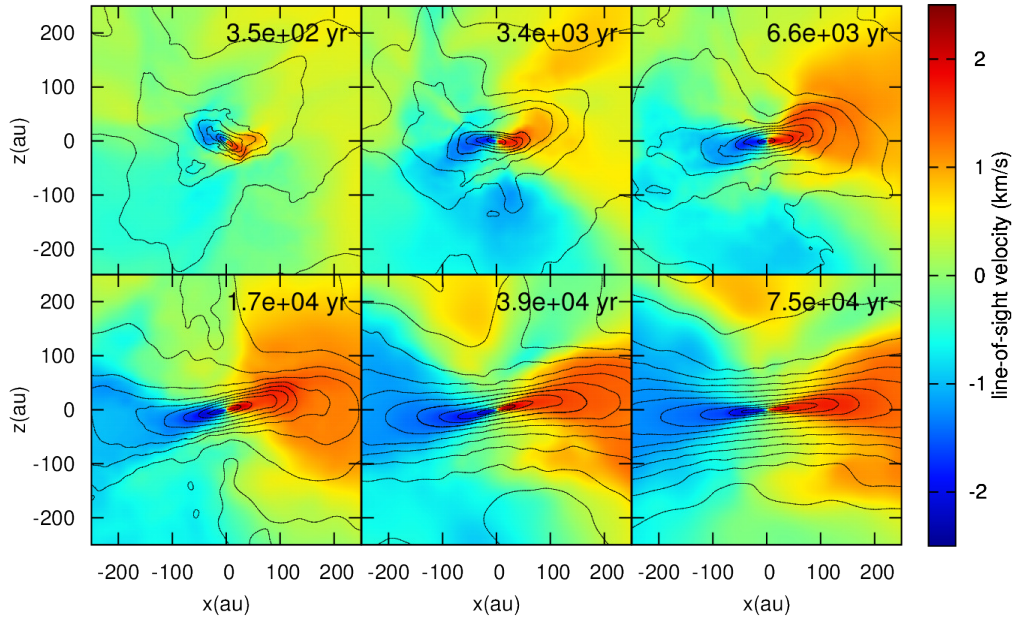


Figure 5. The evolution of the density weighted line-of-sight velocity on the x-z plane for model D4 ($\alpha = 0.5$, $\gamma_{\rm turb} = 0.1$) . The epochs of each panel are the same as Figure 3. Black lines are contours of the surface density.

and they are merged. In models B1 and B3, a binary system with the separation of $\sim$ 30 au and $\sim$ 50 au are formed, respectively. Models B2 and C3 correspond to the triple star formation cases, in which the binary system formed at first and circumbinary disk rotates around them changed into the third object due to the gravitational instability.

Those systems exhibit their own specific but interesting evolution history, and we omit to discuss these results in this paper. Thus, we consider the remaining 20 models in this section.

Figure 8 summarizes the initial ($t \sim 10^2$ yr;blue) and final ($t \sim 10^5$ yr;red) values of $\psi_{\rm sd}$ for 20 models in which the protostar is formed as a single star. Out of the 20 models, 12 models are aligned initially with $\psi_{\rm sd} < 20°$, and the remaining 8 models are misaligned with $\psi_{\rm sd} > 20°$. Figure 1 indicates that $\psi_{\rm sd}$ is barely correlated with α and $\gamma_{\rm turb}$. This is because the initial $\psi_{\rm sd}$ is determined by the local density and velocity fluctuation around the sink particle, while α and $\gamma_{\rm turb}$ characterize the global properties of the entire cloud core. Nevertheless we may recognize a weak positive trend of initial $\psi_{\rm sd}$ and $\gamma_{\rm turb}$ in Figures 1 and 8. On the other hand, the $\psi_{\rm sd}$ is $0° < \psi_{\rm sd} < 20°$ at 10^5 yr after the protostar formation, independently of their initial values.

Figure 9 shows the evolution of $\psi_{\rm sd}$, $M_{\rm s}$ and $\dot{M}_{\rm s}$ of the initially misaligned 8 systems ($\psi_{\rm sd} > 20°$ at $t \sim 10^2$ yr). The top panel shows that the initial values of $\psi_{\rm sd}$ are distributed in $20° < \psi_{\rm sd} < 130°$, and they decrease to $\psi_{\rm sd} < 20°$ in the timescale of several 10^3 yr to 10^4 yr.

The middle panel of Figure 9 shows that the mass increase timescale varies from $\lesssim 10^3$ yr (green solid line) to $\sim 10^4$ yr (green dotted line). As expected from the equation (17), $\psi_{\rm sd}$ of the model with the small mass increase timescale (e.g., green solid line of the middle panel of Figure 9) quickly decreases to $\psi_{\rm sd} < 10°$ in $t < 10^3$ yr. The correlation between the small mass increase timescale and the small alignment timescale suggests that the equation (17) is a good estimate of the alignment timescale of the stellar spin and disk rotation direction. In all models considered in this paper, the final values of $\psi_{\rm sd}$ range from a few to 10° and very small.

Our current simulations predict relatively well-aligned star-disk systems. We note, however, a few cations here before drawing general conclusions. Firstly, we focus on the 20 single star systems, and do not discuss the other six multiple-star systems out of the 26 models summarized in Table 1. Secondly, those 20 systems have massive disks roughly comparable to the central protostar mass as shown in Figure 10. This is consistent with Bate et al. (2010), but not with Fielding et al. (2015). The misaligned systems in Fielding et al. (2015) preferentially have less massive disks, which are likely disturbed by the subsequent accretion from the envelope and/or by the perturbation from a distant star. The single star systems in our simulation neglects the possible interaction with the outer system, and may underestimate the possible evolution toward the star-disk misalignment. Batygin (2012) showed that the gravitational torque due to a distant star significantly affects the orientation of the disk plane relative to the central stellar spin. Finally the sink particle technique is admittedly very approximate and cannot reliably describe the physics inside the accretion radius of the sink particle.

Having said so, however, it is encouraging that our higher-resolution SPH simulations are generally consistent with the previous SPH result by Bate et al. (2010). Furthermore, Fielding et al. (2015) also found a star-disk alignment

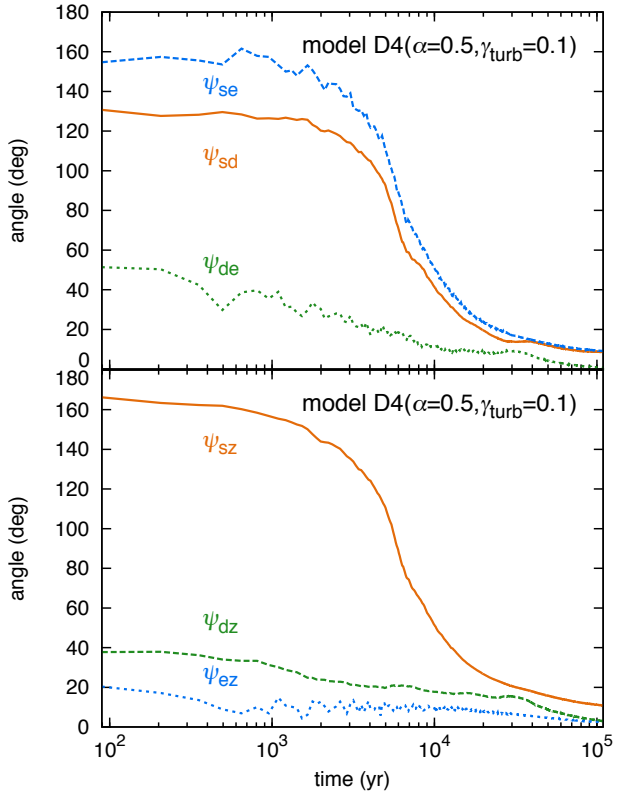


Figure 6. Time evolution of the directions of the stellar spin, disk rotation and envelope rotation for model D4 ($\alpha = 0.5$, $\gamma_{\rm turb} = 0.1$) . The red-solid, blue-dashed and green-dotted lines in the upper panel show star-disk relative angle $\psi_{\rm sd}(t)$, star-envelope relative angle $\psi_{\rm se}(t)$, and disk-envelope relative angle $\psi_{\rm de}(t)$, respectively. The red-solid, green-dashed and blue-dotted lines show the stellar spin angle $\psi_{\rm sz}(t)$, disk rotation angle $\psi_{\rm dz}(t)$ envelope rotation angle $\psi_{\rm ez}(t)$ from z axis.

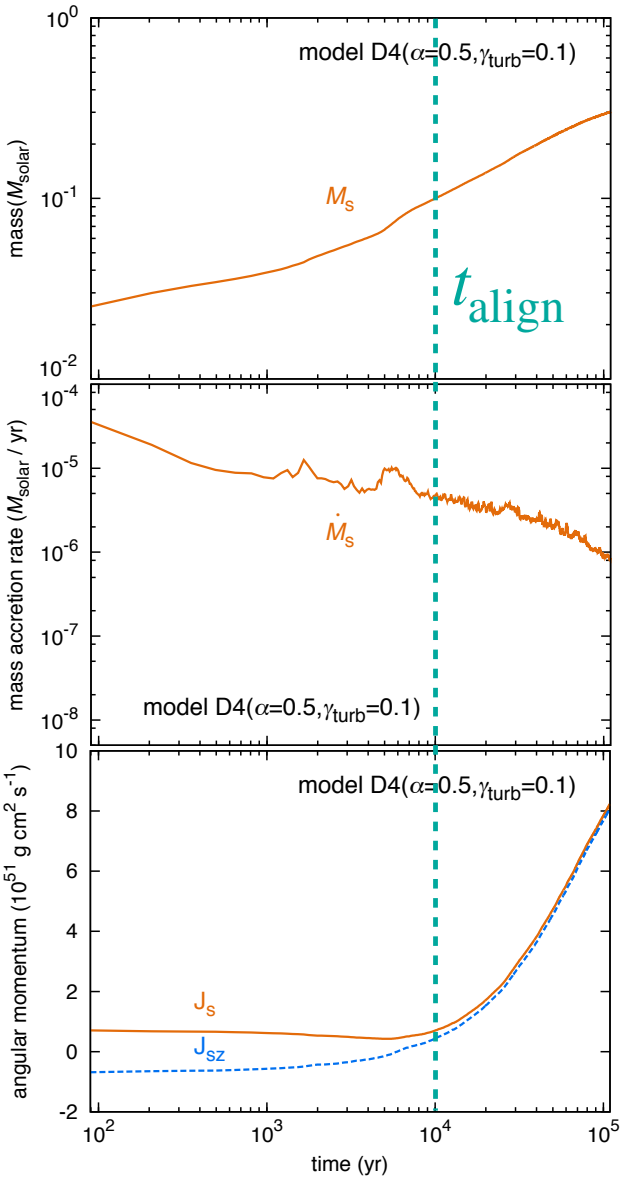


Figure 7. Time evolution of the mass of the protostar (top), mass accretion rate onto the protostar (middle) and spin angular momentum of the protostar (bottom), respectively, for model D4 ($\alpha = 0.5$, $\gamma_{\rm turb} = 0.1$) . The horizontal axis shows the time from the protostar formation.

if the disk mass is comparable to that of the protostar even in their AMR simulation. Thus the star-disk mass ratio may be an important parameter that is responsible for the degree of the primordial star-disk orientation.

5 WARPED DISK AND ENVELOPE ROTATION STRUCTURES

In following two subsection, we examine whether our simulation results can explain recent observations of the warped disk and counter-rotating envelope.

5.1 Warped Disks

Sakai et al. (2019) reported the warped disk-like structure around a young protostar, IRAS 04368+2557, located in the protostellar core L1527 that is classified as a Class 0 YSO. Because such a warped disk is expected to evolve into spin-orbit misaligned planetary systems, their detailed structure may be connected to the observed diversity of the spin-orbit architecture.

We suggest that such a warped disk can be explained by the turbulence in the molecular cloud cores. We show the evolution of the surface density and line-of-sight velocity of model B5 ($\alpha = 0.3$, $\gamma_{\rm turb} = 0.3$) in Figures 11 and 12. Figure 11 shows that the warped structure is formed in $t \lesssim 4 \times 10^4$ yr. In particular, the top right and bottom left panels show the elongation of the surface density and rotation structure. The turbulent accretion flow from the circumstellar envelope causes this warped disk structure.

To examine the warped structure of the protoplanetary disk quantitatively, we plot the angle $\psi_{\rm shell}(r)$ between the angular momentum of the spherical shell and the spin of the protostar,

$$\psi_{\rm shell}(r) = \cos^{-1}\left(\frac{\boldsymbol{J}_{\rm s}\cdot\boldsymbol{J}_{\rm shell}(r)}{|\boldsymbol{J}_{\rm s}||\boldsymbol{J}_{\rm shell}(r)|}\right), \tag{18}$$

where $\boldsymbol{J}_{\rm shell}(r)$ is the angular momentum of the spherical shell at r.

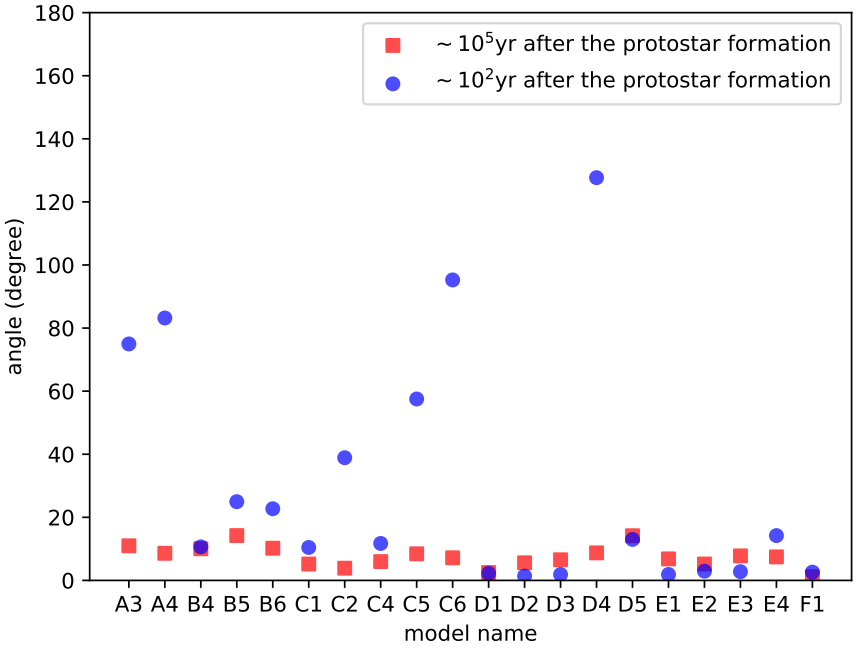


Figure 8. $\psi_{\rm sd}$ at $t \sim 10^2$ yr (blue) and $t \sim 10^5$ yr (red) of different models.

Figure 13 shows the radial profile of $\psi_{\rm shell}(r)$ at different epochs. In all epochs, $\psi_{\rm shell}(r)$ is almost flat in $r < 40$ au. This means that the inner disk in $r < 40$ au is not warped. On the other hand, $\psi_{\rm shell}(r)$ decreases in 40 au < r < 100 au at $t = 2.2 \times 10^4$ yr (orange) and at $t = 4.1 \times 10^4$ yr (green) indicating that the disk is warped in this region. The relative angle between the inner and outer region is $\sim 5^\circ$ at $t = 2.2 \times 10^4$ yr and good agreement with Sakai et al. (2019). This indicates that, with the turbulent infalling envelope, the rotation axis of the inner disk is not necessarily aligned with that of the outer disk and the warped disk is expected in the early evolution phase of YSOs.

Note that the top-left and top-middle panels of Figure 11 show the filamentary structure of the infalling envelope which extends to the z directions. Interestingly, the density weighted line-of-sight velocity of these filaments are both blue (top-left and top-middle of Figure 12), meaning that the accretion flow has the same direction in the upper and lower regions of the disk.

Yen et al. (2014) reported the infalling flows of the envelope in parabolic trajectories toward the Keplerian disk of a Class I protostar, L1489 IRS. The red-shifted and blue-shifted structures in the lower-left and lower-center panels of Figure 12 look very similar to the infalling envelope structure reported in their Figure 3. This suggests that the arc-like structure of infalling envelopes may be naturally formed by the turbulent accretion of the infalling matter in the early phase of YSOs.

5.2 Envelope rotation structure

Takakuwa et al. (2018) found a Class I YSO in which the rotation direction of the circumstellar envelope significantly change from 1000 au scale to inner 100 au scale, which can be interpreted as a counter rotation between the protoplanetary disk and circumstellar envelope. The physical mechanism which induces such a counter-rotating structure is still unclear. One may expect that the random motion of the turbulence may create the random rotation direction of the circumstellar envelope, leading to a counter rotation. However, we do not find such a significant change of the rotation direction in the circumstellar envelope in our simulations. Rather, the protoplanetary disk rotation tends to be aligned with the circumstellar envelope rotation especially in the late phase.

An example is presented in Figure 14 that shows the time evolution of $\psi_{\rm sd}$ and $\psi_{\rm shell}$ at $r = 30$ au (red), 100 au (orange), 300 au (green) and 1000 au (blue), respectively, for model B5 ($\alpha = 0.3$, $\gamma_{\rm turb} = 0.3$) . Even at $t = 10^2$ yr, $\psi_{\rm shell}$ at $r = 1000$ au is $\sim 70^\circ$ and $\psi_{\rm shell}$ is not counter rotating. Subsequently, $\psi_{\rm shell}$ keeps decreasing, instead of increasing, and all the values of $\psi_{\rm shell}$ as well as $\psi_{\rm sd}$ converge to $\sim 15^\circ$. This clearly indicates that the turbulence in molecular cloud cores is unlikely to produce a counter-rotating structure.

The prograde rotation inside an isolated compact region is a generic outcome of the gravitational collapse of turbulent molecular cloud cores. In order to see it, we introduce the relative angle between the angular momenta of the inner shell at $r = 100$ au and the outer shell at $r = 1000$ au:

$$\psi_{\rm shell,\,100\ au-1000\ au} = \cos^{-1}\left(\frac{\boldsymbol{J}_{\rm shell}(100\ {\rm au})\cdot\boldsymbol{J}_{\rm shell}(1000\ {\rm au})}{|\boldsymbol{J}_{\rm shell}(100\ {\rm au})||\boldsymbol{J}_{\rm shell}(1000\ {\rm au})|}\right). \quad (19)$$

Figure 15 shows $\psi_{\rm shell,\,100\ au-1000\ au}$ of all the simulation models with star-disk misalignment ($\psi_{\rm sd} > 20^\circ$ at $t \sim 10^2$ yr). Figure 15 suggests that $\psi_{\rm shell,\,100\ au-1000\ au}$ is $\lesssim 70^\circ$ even

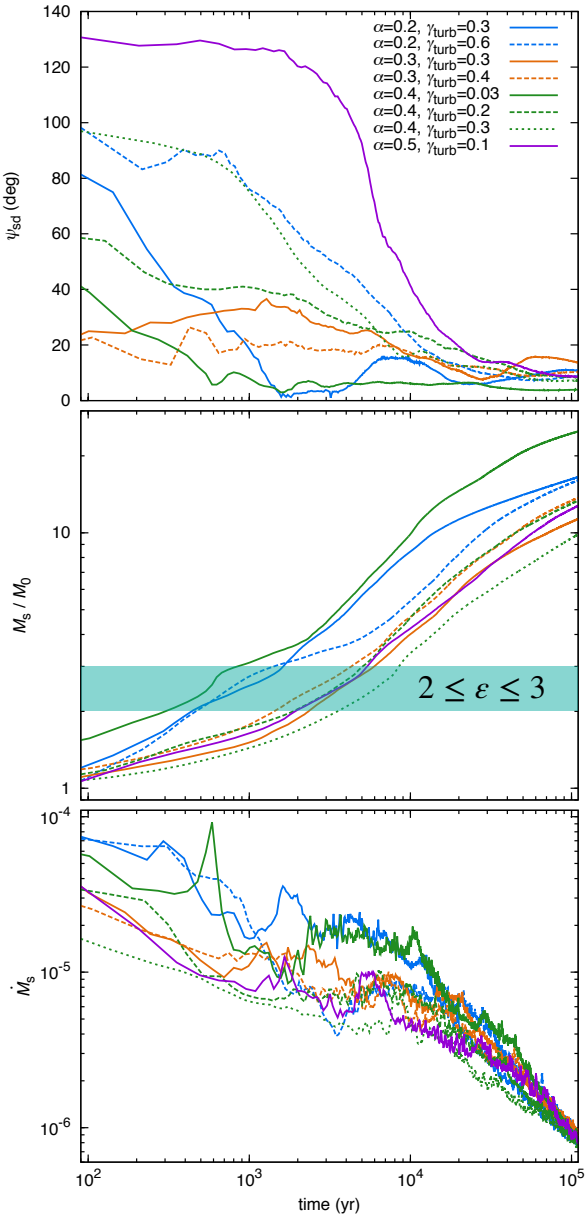


Figure 9. Time evolution of $\psi_{\rm sd}$ (top), protostar mass (middle) and protostar mass accretion rate (bottom) of all simulations in which the star-disk misalignment appeared. The horizontal axis of this plot correspond to the time from the protostar formation. This is the case that the protostar is formed as a single star.

at $t = 10^2$ yr, and then gradually becomes aligned towards $\lesssim 20°$ at $t = 10^5$ yr. Thus, no simulation exhibits the misalignment between the inner envelope ($r \sim 100$ au) and the outer envelope ($r \sim 1000$ au). We compared the angular momentum of the inner shell ($r = 100$ au) with that of the further outer shells (1000 au < r < 3000 au), and confirmed that the counter-rotating envelope does not appear even in the scale of 3000 au.

Thus we conclude that the turbulence in the molecular cloud core may not create a counter-rotating envelope. Rather, the magnetic field in the molecular cloud core may create it (e.g., Krasnopolsky et al. 2011; Li et al. 2011; Tsukamoto et al. 2015c; Wurster et al. 2016; Tsukamoto et al. 2017; Wurster et al. 2017, 2018; Wurster & Bate 2019).

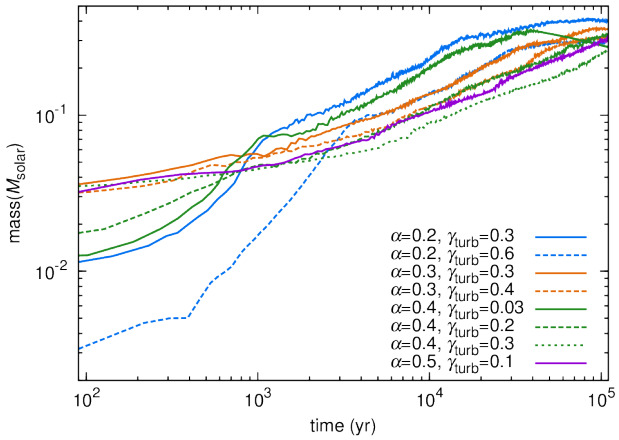


Figure 10. Time evolution of the mass of the protoplanetary disk. We plot the results of our simulations with star-disk misalignment. The horizontal axis of this plot shows the time after the protostar formation.

6 CONCLUSION

Observed exoplanetary systems are known to exhibit diverse properties that are quite different from those of our Solar system. In particular, the presence of the spin-orbit misaligned planetary systems is supposed to carry important information concerning the initial condition of the protoplanetary disk and the subsequent formation and dynamical evolution of multi-planetary systems.

One of the basic questions underlying the spin-orbit architecture is to what extent the spin axis of the protostar and the rotation axis of the protoplanetary disk are aligned. While this question seems well-defined and straightforward, it is not easy to give an unambiguous answer because a variety of complicated physical processes of very different spatial and time scales are involved. Indeed, a pioneering work by Bate et al. (2010) indicates that the star-disk angle of the protoplanetary disk systems out of supersonic turbulent clouds can be significantly misaligned, but that the reliable prediction is not easy because the process occurs in an inherently chaotic environment.

We have performed the SPH simulation of the collapse of turbulent molecular cloud cores with varying the thermal and turbulent energy contributions relative to the gravitational energy of those systems. This paper has focused on the analysis of 20 single star-forming systems out of the 26 models in total. Our major findings are summarized as follows.

1. At the initial phase of the protostar formation, the axis of the stellar spin is not necessarily aligned with that of the disk rotation. The star-disk angle $\psi_{\rm sd}$ is almost randomly distributed within $\sim 130°$ until $\sim 10^4$ yr after the protostar formation.
2. The subsequent mass accretion from the disk to the protostar gradually aligns the stellar spin toward the disk rotation axis. The disk also receives the angular momentum accretion from the surrounding envelope, and its rotation axis becomes aligned to that of the initial angular momentum of the cloud core. As a result, $\psi_{\rm sd}$ becomes less than $\sim 20°$ in $\sim 10^4$ yr after the protostar formation. The timescale of

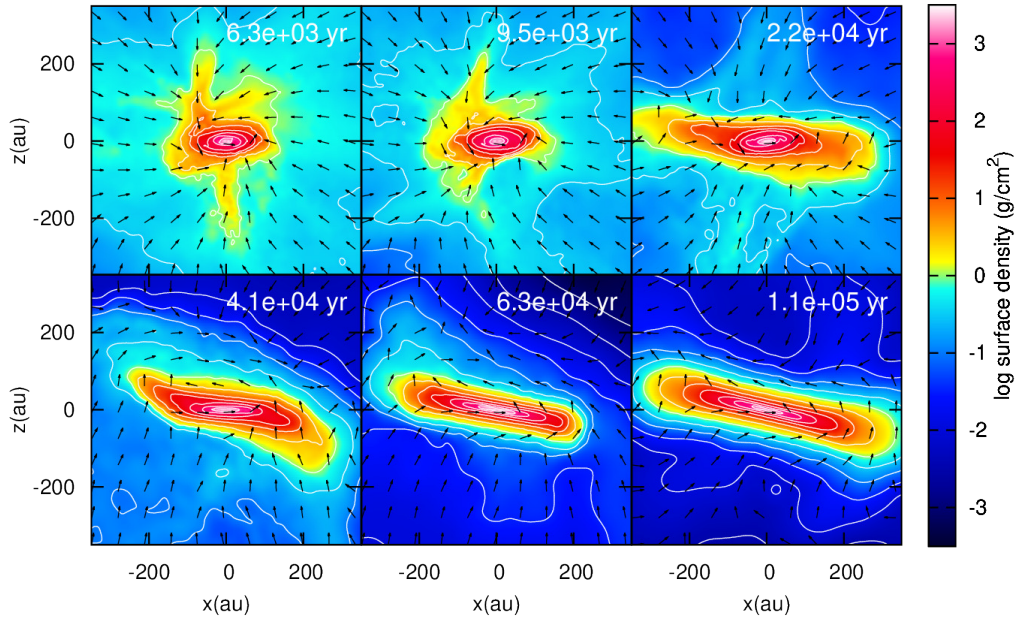


Figure 11. The surface density evolution on the x-z plane for model B5 (α = 0.3, $\gamma_{\rm turb}$ = 0.3) . The top-left, top-middle and top-right panels show snapshots at 6.3×10^3 yr, 9.5×10^3 yr and 2.2×10^4 yr after the protostar formation, respectively. The bottom-left, bottom-middle and bottom-right panels show snapshots at 4.1×10^4 yr, 6.3×10^4 yr and 1.1×10^5 yr after the protostar formation, respectively. White lines show contours of the surface density. Black arrows show direction of the density weighted velocity.

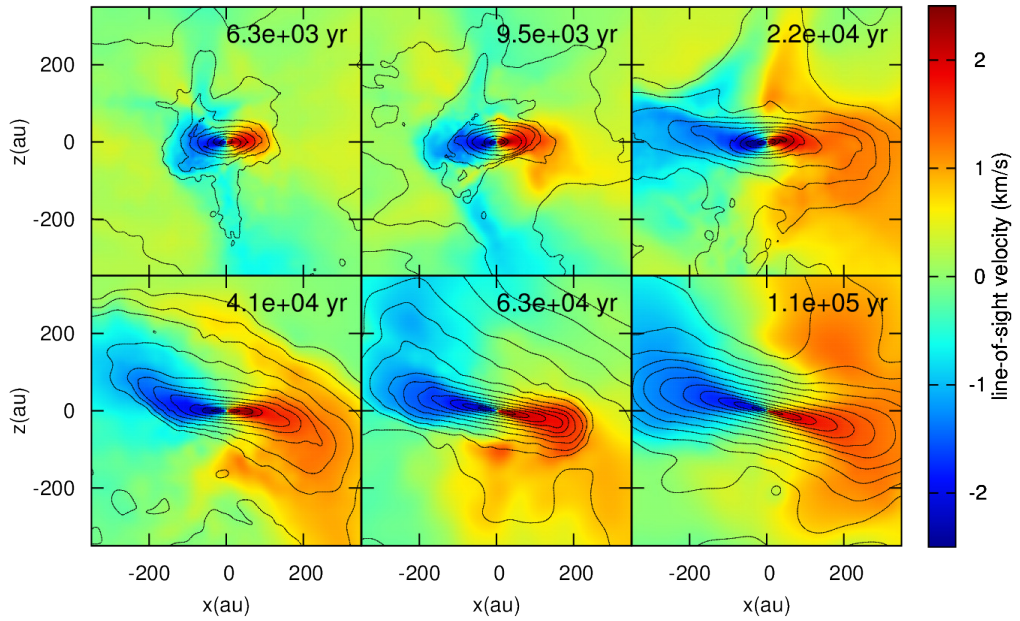


Figure 12. The evolution of the density weighted line-of-sight velocity on the x-z plane for model B5 (α = 0.3, $\gamma_{\rm turb}$ = 0.3) . The epochs of each panel are the same as Figure 11. Black lines are contours of the surface density.

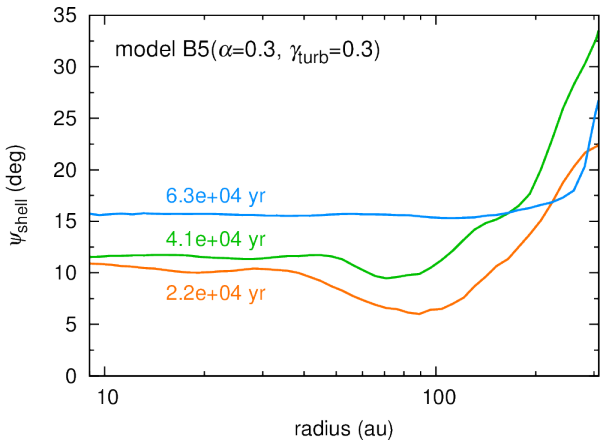


Figure 13. Radial distribution of $\psi_{\rm shell}$ for model B5 (α = 0.3, $\gamma_{\rm turb}$ = 0.3) . Orange, green, and blue lines correspond to $\psi_{\rm shell}$ at 2.2×10^4 yr, 4.1×10^4 yr, and 6.3×10^4 yr after the protostar formation, respectively.

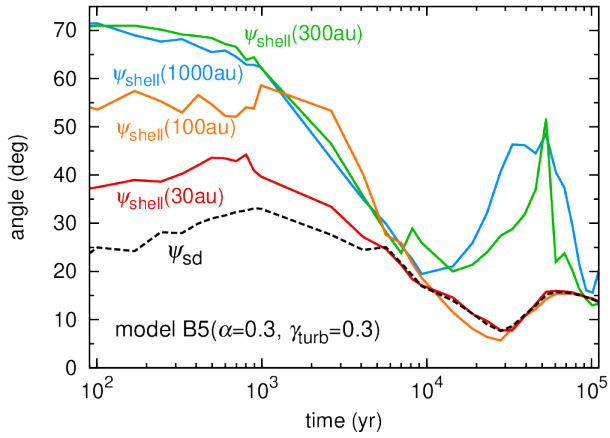


Figure 14. Time evolution of $\psi_{\rm sd}$ and $\psi_{\rm shell}$ for model B5 (α = 0.3, $\gamma_{\rm turb}$ = 0.3) . Red, orange, green, and blue lines correspond to the $\psi_{\rm shell}$ at r = 30 au, 100 au, 300 au, and 1000 au, respectively. Dashed black line shows $\psi_{\rm sd}$.

the star-disk alignment, $t_{\rm alignment} \sim 10^4$ yr corresponds to a typical mass doubling time of the central protostar.

3. The star-disk angles $\psi_{\rm sd}$, measured at the epoch of the protostar formation (about $t = 10^2$ yr) and the end of our simulations ($t = 10^5$ yr) are insensitive to $\alpha = E_{\rm thermal}/|E_{\rm gravity}|$ nor to $\gamma_{\rm turb} = E_{\rm turbulence}/|E_{\rm gravity}|$.

4. Our simulation sometimes produces a warped disk structure as recently reported by Sakai et al. (2019). A clear warped structure is produced when the mass accretion and angular momentum transfer from the envelope to the outer disk proceeds along the direction significantly different from that of the existing inner disk. This process also changes the rotation axis of the inner disk gradually, and $\psi_{\rm sd}$ fluctuates by an amount of $\sim 10^\circ$ even after it once becomes less than 20°.

5. Rotation directions of the disk and envelope are generally well aligned, especially after the significant mass accretion ceases ($t \sim 10^5$ yr). Therefore the turbulence of the molecular cloud cores alone does not lead to a counter-rotating disk structure.

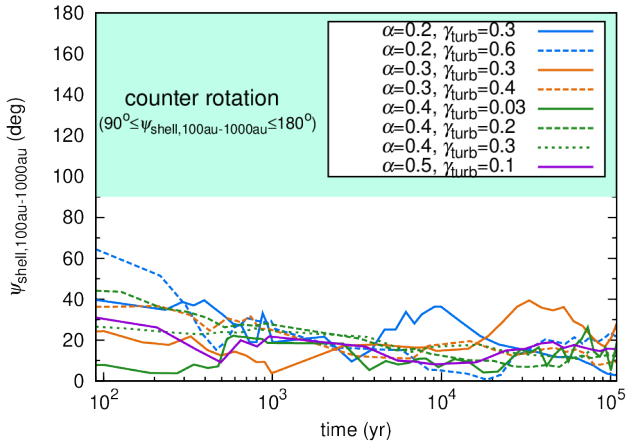


Figure 15. Time evolution of $\psi_{\rm shell,100\ au-1000\ au}$ for all the simulation models with $\psi_{\rm sd} > 20^\circ$ at $t \sim 10^2$ yr. The shaded region corresponds to a counter-rotating structure ($90^\circ \leq \psi_{\rm shell,100\ au-1000\ au} \leq 180^\circ$).

Our overall conclusion is that the stellar spin and disk rotation axes of a protoplanetary disk system out of a turbulent cloud core are aligned less than $\sim 20^\circ$. We should emphasize, however, that this conclusion holds only for an isolated single star-forming case. If the initial cloud core has sufficiently massive and its thermal and turbulent energies are smaller than the gravitational energy, it would preferentially produce multiple protoplanetary disks inside (see Figure 1). Then the star-disk angle of a planetary system can be significantly affected by the perturbation from a nearby system as proposed by Batygin (2012), for instance. Furthermore, the magnetic field, which is neglected in the present simulation, may also play an important role. More realistic simulations including the magnetic field and turbulence simultaneously are numerically demanding and expensive, but we plan to perform and hope to report the result in a future work.

ACKNOWLEDGEMENTS

We thank an anonymous referee for a number of important and constructive comments that significantly improved the earlier manuscript of the paper. Numerical computations were in part carried out on Cray XC50 at Center for Computational Astrophysics, National Astronomical Observatory of Japan. This research is supported by JSPS (Japan Society of Promotion of Science) Core-to-Core Program "International Network of Planetary Sciences", by the Astrobiology Center of National Institutes of Natural Sciences (NINS) Grant Number AB311025, and also by JSPS KAKENHI Grant Numbers 18H01247 (Y.S.), 18H05437 (Y.T.), 18K13581 (Y.T.), and 19H01947 (Y.S.).

REFERENCES

Albrecht S., et al., 2012, ApJ, 757, 18

Albrecht S., Winn J. N., Marcy G. W., Howard A. W., Isaacson H., Johnson J. A., 2013, ApJ, 771, 11
Alibert Y., Mordasini C., Benz W., Winisdoerffer C., 2005, A&A, 434, 343
Anderson K. R., Storch N. I., Lai D., 2016, MNRAS, 456, 3671
Andre P., Ward-Thompson D., Motte F., 1996, A&A, 314, 625
Barranco J. A., Goodman A. A., 1998, ApJ, 504, 207
Bate M. R., 2018, MNRAS, 475, 5618
Bate M. R., Burkert A., 1997, MNRAS, 288, 1060
Bate M. R., Bonnell I. A., Price N. M., 1995, MNRAS, 277, 362
Bate M. R., Lodato G., Pringle J. E., 2010, MNRAS, 401, 1505
Batygin K., 2012, Nature, 491, 418
Beaugé C., Nesvorný D., 2012, ApJ, 751, 119
Bertoldi F., McKee C. F., 1992, ApJ, 395, 140
Burkert A., Bodenheimer P., 2000, ApJ, 543, 822
Butler M. J., Tan J. C., 2012, ApJ, 754, 5
Crutcher R. M., Nutter D. J., Ward-Thompson D., Kirk J. M., 2004, ApJ, 600, 279
Fabrycky D., Tremaine S., 2007, ApJ, 669, 1298
Fielding D. B., McKee C. F., Socrates A., Cunningham A. J., Klein R. I., 2015, MNRAS, 450, 3306
Gingold R. A., Monaghan J. J., 1977, MNRAS, 181, 375
Goodman A. A., Benson P. J., Fuller G. A., Myers P. C., 1993, ApJ, 406, 528
Hillenbrand L. A., 1997, AJ, 113, 1733
Hirano T., Suto Y., Winn J. N., Taruya A., Narita N., Albrecht S., Sato B., 2011, ApJ, 742, 69
Hirano T., et al., 2012, ApJ, 759, L36
Huber D., et al., 2013, Science, 342, 331
Inutsuka S., 2012, Progress of Theoretical and Experimental Physics, 2012, 01A307
Kamiaka S., Benomar O., Suto Y., Dai F., Masuda K., Winn J. N., 2019, AJ, 157, 137
Kozai Y., 1962, AJ, 67, 591
Krasnopolsky R., Li Z.-Y., Shang H., 2011, ApJ, 733, 54
Li Z.-Y., Krasnopolsky R., Shang H., 2011, ApJ, 738, 180
Lidov M. L., 1962, Planet. Space Sci., 9, 719
Lin D. N. C., Bodenheimer P., Richardson D. C., 1996, Nature, 380, 606
Lucy L. B., 1977, AJ, 82, 1013
Machida M. N., Inutsuka S., Matsumoto T., 2007, ApJ, 670, 1198
Machida M. N., Inutsuka S., Matsumoto T., 2010, ApJ, 724, 1006
Machida M. N., Inutsuka S., Matsumoto T., 2014, MNRAS, 438, 2278
Masunaga H., Inutsuka S., 2000, ApJ, 531, 350
McKee C. F., Ostriker E. C., 2007, ARA&A, 45, 565
McLaughlin D. B., 1924, ApJ, 60, 22
Miyama S. M., Hayashi C., Narita S., 1984, ApJ, 279, 621
Monaghan J. J., Lattanzio J. C., 1985, A&A, 149, 135
Nagasawa M., Ida S., 2011, ApJ, 742, 72
Nagasawa M., Ida S., Bessho T., 2008, ApJ, 678, 498
Ohta Y., Taruya A., Suto Y., 2005, ApJ, 622, 1118
Queloz D., Eggenberger A., Mayor M., Perrier C., Beuzit J. L., Naef D., Sivan J. P., Udry S., 2000, A&A, 359, L13
Rasio F. A., Ford E. B., 1996, Science, 274, 954
Rossiter R. A., 1924, ApJ, 60, 15
Sakai N., Hanawa T., Zhang Y., Higuchi A. E., Ohashi S., Oya Y., Yamamoto S., 2019, Nature, 565, 206
Shu F. H., 1977, ApJ, 214, 488
Tafalla M., Mardones D., Myers P. C., Caselli P., Bachiller R., Benson P. J., 1998, ApJ, 504, 900
Takakuwa S., Tsukamoto Y., Saigo K., Saito M., 2018, ApJ, 865, 51
Triaud A. H. M. J., 2018, The Rossiter-McLaughlin Effect in Exoplanet Research. p. 2, doi:10.1007/978-3-319-55333-7_2
Tsukamoto Y., Machida M. N., 2011, MNRAS, 416, 591
Tsukamoto Y., Machida M. N., 2013, MNRAS, 428, 1321
Tsukamoto Y., Machida M. N., Inutsuka S., 2013, MNRAS, 436, 1667
Tsukamoto Y., Takahashi S. Z., Machida M. N., Inutsuka S., 2015a, MNRAS, 446, 1175
Tsukamoto Y., Iwasaki K., Okuzumi S., Machida M. N., Inutsuka S., 2015b, MNRAS, 452, 278
Tsukamoto Y., Iwasaki K., Okuzumi S., Machida M. N., Inutsuka S., 2015c, ApJ, 810, L26
Tsukamoto Y., Okuzumi S., Iwasaki K., Machida M. N., Inutsuka S., 2017, Publications of the Astronomical Society of Japan, 69, 95
Tsukamoto Y., Okuzumi S., Iwasaki K., Machida M. N., Inutsuka S., 2018, ApJ, 868, 22
Ward-Thompson D., André P., Crutcher R., Johnstone D., Onishi T., Wilson C., 2007, in Reipurth B., Jewitt D., Keil K., eds, Protostars and Planets V. p. 33 (arXiv:astro-ph/0603474)
Williams J. P., Myers P. C., Wilner D. J., Di Francesco J., 1999, ApJ, 513, L61
Winn J. N., Fabrycky D. C., 2015, ARA&A, 53, 409
Winn J. N., et al., 2005, ApJ, 631, 1215
Wurster J., Bate M. R., 2019, MNRAS, p. 933
Wurster J., Price D. J., Bate M. R., 2016, MNRAS, 457, 1037
Wurster J., Price D. J., Bate M. R., 2017, MNRAS, 466, 1788
Wurster J., Bate M. R., Price D. J., 2018, MNRAS, 475, 1859
Xue Y., Suto Y., 2016, ApJ, 820, 55
Xue Y., Suto Y., Taruya A., Hirano T., Fujii Y., Masuda K., 2014, ApJ, 784, 66
Yamamoto S., 2017, Introduction to Astrochemistry: Chemical Evolution from Interstellar Clouds to Star and Planet Formation, doi:10.1007/978-4-431-54171-4.
Yen H.-W., et al., 2014, ApJ, 793, 1
Yen H.-W., Koch P. M., Takakuwa S., Krasnopolsky R., Ohashi N., Aso Y., 2017, ApJ, 834, 178
Yoneda H., Tsukamoto Y., Furuya K., Aikawa Y., 2016, ApJ, 833, 105

APPENDIX A: NUMERICAL CONVERGENCE TEST WITH RESPECT TO THE DIFFERENT MASS, REALIZATION OF TURBULENCE, AND NUMBER OF SPH PARTICLES

In this appendix, we discuss whether the factors which are not considered in this paper change our conclusion or not. For this purpose, we performed the simulations with (1) the different realization of the turbulence, (2) the different mass ($0.3\,M_\odot, 3\,M_\odot$), and (3) the different number of the SPH particles of the initial cloud core for our fiducial model D4 ($\alpha = 0.5$, $\gamma_{\rm turb} = 0.1$) .

Figure A1 summarize our results. At first, we check the impact of the different realization of the turbulence of the initial cloud core. In this study, we only consider one realization of the turbulence for one parameter set of α and $\gamma_{\rm turb}$. However, due to its stochastic nature, the different realization may causes the different conclusions. The green solid line in Figure A1 plots the time evolution of $\psi_{\rm sd}$ with the same parameters of our fiducial model D4 ($\alpha = 0.5$, $\gamma_{\rm turb} = 0.1$) but varying the realization of the turbulence (model Seed2) and shows that the initial star-disk angle $\psi_{\rm sd}$ is much smaller than that of model D4. This is not surprising because the different realization of the turbulence changes the initial distribution of the angular momentum around the protostar. Thus the stellar spin direction at its formation epoch is significantly affected by the realization. Note however, that $\psi_{\rm sd}$ converged to less than 20° due to the

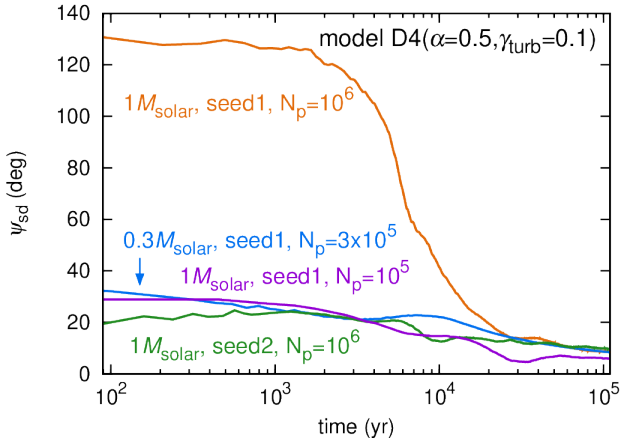


Figure A1. Time evolution of $\psi_{\rm sd}$ for our fiducial model D4 (α = 0.5, $\gamma_{\rm turb}$ = 0.1) in which the mass, realization of the turbulence, and number of SPH particles of the initial cloud core are different.

mechanism discussed in section 3, and our main conclusion is not changed by the random nature of the turbulence.

Next, we check the impact of the mass of the initial cloud core. We conducted here two simulations with the parameters of our fiducial model D4 (α = 0.5, $\gamma_{\rm turb}$ = 0.1) but varying the mass of the initial cloud core as 0.3 $M_\odot$ (model Small) and 3 $M_\odot$ (model Large).

One protostar is formed in model Small, and a binary system is formed in model Large. Blue solid line in Figure A1 shows the time evolution of $\psi_{\rm sd}$ of model Small in which the mass of the initial cloud core is 0.3 $M_\odot$ and shows that while the initial star-disk angle $\psi_{\rm sd}$ of the different mass of 0.3 $M_\odot$ is smaller than that of model D4, it also converged to less than 20°, and there is no significant misalignment of the star-disk angle $\psi_{\rm sd}$ of model Small at $t \sim 10^5$ yr. Therefore our main conclusion is still maintained with this calculation.

A wide binary system with separation $\sim$ 100 au is formed in model Large. Because we will focus on the isolated systems in this work, we do not discuss the result of model Large here. Note, however, that the multiplicity strongly depends on the mass of the cloud core even with the same parameter of α and $\gamma_{\rm turb}$.

Finally, we check the impact of the numerical resolution. For this purpose, we conducted a simulation with the parameters of our fiducial model D4 (α = 0.5, $\gamma_{\rm turb}$ = 0.1) but varying the number of the SPH particles of the initial cloud core as $N_{\rm p} \sim 10^5$ (model Low).

Violet solid line in Figure A1 plots the time evolution of $\psi_{\rm sd}$ of model Low and shows that the initial star-disk angle $\psi_{\rm sd}$ of model Low is also smaller than that of model D4 likewise the case of the model Seed2, and it also converged to less than 20°. It may be related to the change of the interpolation of the initial turbulent velocity field caused by the different initial resolution. The star-disk angle $\psi_{\rm sd}$ also converges to less than 20° in $\sim 10^4$ yr after the protostar formation. Therefore, our main conclusion is still maintained with the smaller numerical resolution.

This paper has been typeset from a TEX/LATEX file prepared by the author.

Table A1. Initial parameters of the molecular cloud cores for the calculations in Appendix A; $\beta_{\rm eff}$ is the dimensionless angular momentum, $R_{\rm init}$, $M_{\rm init}$, and $\rho_{\rm init} = 3M_{\rm init}/(4\pi R_{\rm init}^3)$ are the initial radius, mass, and density of the initial cloud cores. Seed (a random number) is used for the implementation of the initial turbulent velocity field. $\mathcal{M}$ is the initial Mach number, $t_{\rm ff} = \sqrt{3\pi/(32G\rho_{\rm init})}$ is the free-fall time and $N_{\rm p}$ is the number of SPH particles of the initial cloud core. $\psi_{\rm sd}(t = 10^2{\rm yr})$ and $\psi_{\rm sd}(t = 10^5{\rm yr})$ which are the star-disk angles at $t = 10^2$ yr and $t = 10^5$ yr are listed in the third from the end and penultimate columns, respectively. The last column indicates the multiplicity of the protostars in our simulations.

Model	$\beta_{\rm eff}$	$R_{\rm init}$ [au]	$M_{\rm init}$	$\rho_{\rm init}$ [g cm^{-3}]	seed	$\mathcal{M}$	$t_{\rm ff}$ [yr]	$N_{\rm p}$	$\psi_{\rm sd}(t = 10^2{\rm yr})$	$\psi_{\rm sd}(t = 10^5{\rm yr})$	multiplicity
D4	0.012	4917	$1\,M_\odot$	1.2×10^{-18}	seed1	0.77	6.1×10^4	$1,045,414 \approx 10^6$	127.7°	8.7°	single
Seed2	0.012	4917	$1\,M_\odot$	1.2×10^{-18}	seed2	0.77	6.1×10^4	$1,045,414 \approx 10^6$	22.3°	9.9°	single
Low	0.012	4947	$1\,M_\odot$	1.2×10^{-18}	seed1	0.77	6.1×10^4	$104,470 \approx 10^5$	28.9°	6.1°	single
Small	0.0011	1475	$0.3\,M_\odot$	1.3×10^{-17}	seed1	0.77	1.8×10^4	$313,858 \approx 3\times10^5$	30.1°	8.6°	single
Large	0.059	14750	$3\,M_\odot$	1.3×10^{-19}	seed1	0.77	1.8×10^5	$3,140,355 \approx 3\times10^6$		-	binary